

# Self-Tracking Solar Concentrator with Absorption of Diffuse Sunlight

Julia S. van der Burgt, Susan A. Rigter, Nelson de Gaay Fortman, and Erik C. Garnett\*

The highest solar cell efficiencies are obtained with concentrating systems. However, these systems have two major drawbacks: solar tracking is needed and diffuse sunlight is poorly absorbed. Here, a system that overcomes both limitations is presented, by exploiting light-induced halide segregation in mixed halide perovskite films. A monolayer of silica microspheres focuses direct sunlight in a mixed halide perovskite film below. Through light-induced phase segregation a low bandgap region forms in the focal point. Together with funneling of excited states toward the low bandgap regions, this results in a voltage increase characteristic for concentrating systems. Diffuse sunlight is still absorbed by the high bandgap material, avoiding the loss of diffuse sunlight characteristic for conventional concentrators. The formation of low bandgap regions in the perovskite is dynamic, and can follow the position of the focus as the sun moves throughout the day, making solar tracking unnecessary. With detailed optical and electrical simulations, it is shown that this concept can lead to an increase in both voltage and current. This leads to a 6.6% absolute increase in power conversion efficiency compared to the film without microspheres. Absorption and emission measurements confirm the concentration effect, showing the promising potential for a self-optimizing concentrating system.

## 1. Introduction

Concentrator photovoltaics are the record holders in photovoltaic efficiency.<sup>[1]</sup> However, for practical applications, these systems have two major limitations. The first is the need for solar tracking, which leads to bulky and expensive mechanical systems. The second problem is the fact that diffuse sunlight

is not efficiently absorbed in concentrating systems. In most terrestrial applications, the loss in absorption due to the presence of diffuse sunlight completely counteracts the efficiency gain due to concentration.<sup>[2]</sup> In this work, we present a new concentrating solar cell that automatically tracks the sun without the presence of mechanical systems and is able to collect the majority of diffuse light, overcoming the two major limitations of modern-day concentrators.

To overcome the limitations in diffuse sunlight absorption, a system is needed that can absorb and concentrate both direct and diffuse sunlight. In our approach, lenses focus direct sunlight into vertical pillars of low bandgap regions embedded in a high bandgap matrix. Diffuse sunlight is absorbed in the high bandgap matrix and subsequently the excited states are funneled to the low bandgap regions. This electronic concentration of charges results in an effective concentration of diffuse sunlight, which is thermodynamically allowed and driven by

the difference in bandgap.<sup>[3]</sup> This concept is shown schematically in **Figure 1**.

A self-aligning lens-emitter system is desirable in order to simplify fabrication and avoid the need for solar tracking. Our design achieves this goal using absorber films that undergo light-driven phase separation to form low bandgap regions. Microsphere lenses placed on top of the film accept light from any angle of incidence and focus it into different spatial locations depending on the incident angle. Therefore, as the sun moves during the day, the phase-separated (low bandgap) region also moves to automatically stay at the focus, leading to a self-tracking system. Diffuse sunlight, coming from any other angle, will still be absorbed by the high-bandgap material. This approach requires the absorber film to phase separate to form lower bandgap regions under the high intensity focused direct sunlight but also to remix under low intensity diffuse sunlight to reform the higher bandgap matrix. The kinetics of phase separation and remixing also need to be sufficiently fast to track the sun (minutes to hours timescale).

Mixed halide perovskites are an excellent candidate material for the absorber film in our self-tracking and diffuse light utilizing solar concentrator. Halide perovskite thin films are in general good candidates for efficient solar cell devices, surpassing all expectations in terms of solar cell efficiency over

J. S. van der Burgt, S. A. Rigter, N. de Gaay Fortman, E. C. Garnett

Center for Nanophotonics

AMOLF

Science Park 104, Amsterdam 1098XG, The Netherlands


S. A. Rigter, N. de Gaay Fortman, E. C. Garnett

Institute of Physics

University of Amsterdam

Science Park 904, Amsterdam 1098XH, The Netherlands

E-mail: e.c.garnett@uva.nl

 The ORCID identification number(s) for the author(s) of this article can be found under <https://doi.org/10.1002/adom.202202013>.

© 2023 The Authors. Advanced Optical Materials published by Wiley-VCH GmbH. This is an open access article under the terms of the Creative Commons Attribution License, which permits use, distribution and reproduction in any medium, provided the original work is properly cited.

DOI: 10.1002/adom.202202013

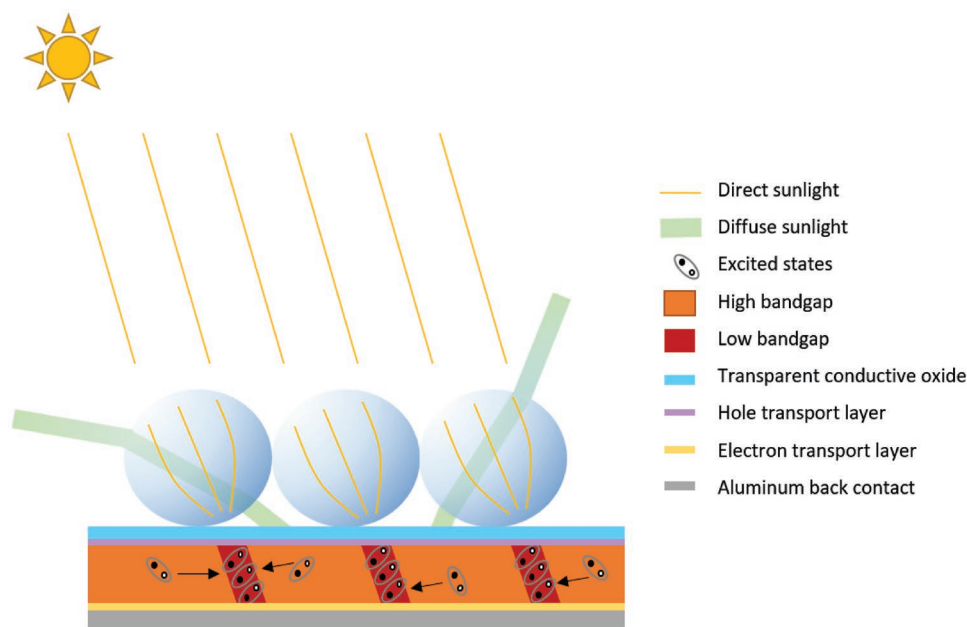


**Figure 1.** Schematic representation of the self-tracking solar concentrator with absorption of diffuse sunlight. Microspheres focus the direct sunlight to a hotspot in the underlying film. In the hotspot a low bandgap material is formed, where excited states get concentrated. Diffuse sunlight from any direction is absorbed in the high bandgap matrix and the resulting excited states are funneled to the low bandgap regions. The position of the hotspot, and thereby of the low bandgap phase, moves along with the motion of the sun.

the past decade.<sup>[1]</sup> Their facile processability, strong absorption, and long carrier diffusion lengths are a few of their most attractive qualities for photovoltaics.<sup>[4–6]</sup> Additionally, one of their core qualities is that the bandgap of the material can be tuned by mixing halides, where a combination of bromide and iodide can give the highest efficiency single-junction solar cell.<sup>[7]</sup> Importantly for our design, under illumination, the uniform alloy of bromide and iodide tends to segregate into iodide- and bromide-rich regions, with respectively lower and higher bandgaps. When left in the dark, the film remixes, with kinetics that depend on both the illumination intensity and composition.<sup>[8,9]</sup> Halide segregation has been considered a limitation, as without additional measures this segregation reduces photovoltaic efficiency.<sup>[7,10]</sup> This reduced efficiency is a consequence of carriers funneling toward the low bandgap regions, by which the recombination, and thus the dark recombination current ( $J_0$ ) and the open circuit voltage ( $V_{oc}$ ) become fully determined by the low bandgap phase.<sup>[11]</sup> However, for the system described above, halide segregation is exactly the desired behavior. It has already been shown that the increased carrier concentration due to funneling toward the low bandgap regions promotes radiative recombination, which partly counteracts the loss in  $V_{oc}$  caused by the lower bandgap.<sup>[11]</sup> By placing microlenses on top of the mixed halide perovskite film, the phase segregation happens in a controlled manner, namely in the hotspots of the microlenses. This concentrates direct sunlight selectively in the lower bandgap perovskite, allowing for high absorption in the lower energy spectral range even when only a few percent of the film is phase separated, as will be shown later.

We chose to use silica microspheres for our self-tracking microlenses because they can be processed on larger scales and

accept light from any angle of incidence. They can focus light to produce photonic nanojets<sup>[12,13]</sup> that create a hotspot underneath the spheres. They can be easily synthesized with various sizes and excellent monodispersity,<sup>[14]</sup> and subsequently assembled in large-scale arrays of hexagonally packed spheres.<sup>[15]</sup> With a monolayer of microspheres on top of a mixed halide perovskite film, the system as depicted in Figure 1 can be achieved. Assuming the iodide-rich regions extend from the top to the bottom contact, the carriers can be collected for all lateral positions of the low bandgap regions and thus for any sunlight incident angle.

In this work, we analyze our design for a self-tracking, diffuse light accepting solar concentrator and quantify its performance. We use optical simulations to determine the effect of halide segregation in combination with focusing spheres on solar cell absorption. The resulting photocarrier generation profiles are used as an input for detailed balance calculations and electrical simulations of a full solar cell device to determine the performance of our design compared to conventional perovskite solar cell architectures. We find that implementing microsphere lenses greatly improves performance of phase separated films and even slightly outperforms stable films. Furthermore, we demonstrate an experimental proof-of-concept by assembling arrays of hexagonally packed spheres on a mixed halide perovskite thin film. Changes in absorption and emission directivity due to the presence of the spheres are in agreement with the simulations. This concept of combining the light focusing properties of silica microspheres with the dynamic nature of mixed halide perovskites, can overcome the limitations of both concentrator systems and mixed halide perovskite solar cells, which opens up a new pathway to high-efficiency perovskite solar concentrators.

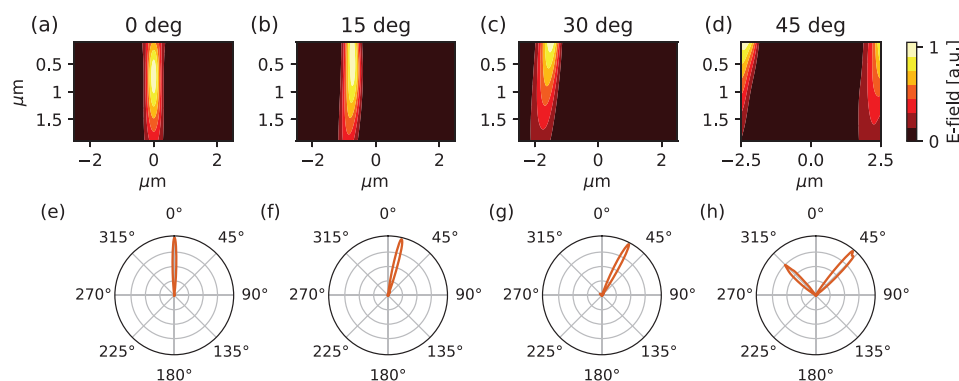


**Figure 2.** Optical simulation results of 5  $\mu\text{m}$  silica spheres on a glass substrate. Top row: electric field intensity in the substrate underneath the center of the sphere for plane wave illumination with increasing angle of incidence. Bottom row: far-field emission pattern from a dipole source placed at the position of maximum field intensity in plane wave illumination. The emission is beaming back into the direction of the incident field due to laws of reciprocity. At 45°, the emitter starts to couple to the neighboring sphere, and part of the emission is beamed into the opposite direction.

## 2. Results and Discussion

### 2.1. Simulations

Finite-difference time domain (FDTD) simulations were used to investigate the focusing characteristics of both individual silica microspheres and closed-packed arrays. When a single glass sphere is illuminated with a plane wave at normal incidence, a strong field enhancement, a nanojet, is observed in the substrate underneath the center of the sphere (Figure 2a). The location of the nanojet dictates where a localized iodide-rich perovskite emitter is formed. To investigate the concentration effect, we use a measure called directivity, which is defined as the light emission in a given angle divided by the average light emission over all angles. The directivity of light emission is thermodynamically equivalent to the concentration factor, but is easier to verify experimentally and for nanoscale systems has a more robust connection to efficiency gains associated with light concentration.<sup>[2,16,17]</sup> The emission pattern resulting from a dipole emitter in the center of the nanojet shows narrow beaming into the upward direction (Figure 2e). Directivity rapidly increases with sphere size, due to the increasing quality factor of the cavity (the sphere), as summarized in Table 1. The ideal size of the spheres is a trade-off between maximizing directivity (optical concentration) and still allowing for diffusion of photogenerated carriers from the high bandgap matrix to the low bandgap region at the focus (electronic concentration). If the spheres become larger than the carrier diffusion length, then electronic concentration drops and diffuse light may not be collected as efficiently. All further simulations are done on 5  $\mu\text{m}$  diameter spheres, mostly motivated by the commercial availability of this size for experimental verification. Potentially,

**Table 1.** Directivity from silica microspheres on a glass substrate, using a dipole emitter located at the center of the hotspot that is formed when illuminated with a plane wave at normal incidence. Directivity increases with sphere size, due to increasing quality factor.

Sphere radius	2 $\mu\text{m}$	3 $\mu\text{m}$	4 $\mu\text{m}$	5 $\mu\text{m}$	6 $\mu\text{m}$	8 $\mu\text{m}$	10 $\mu\text{m}$
Directivity	20	30	40	51	80	97	153

the ideal size is larger because perovskites are known for their long diffusion lengths up to tens of micrometers. Simulations of 5  $\mu\text{m}$  diameter spheres in a hexagonal array yield the same pattern of a single focus underneath each sphere for plane wave excitation, and the same emission pattern from a dipole at the focus in the center of the array. This indicates that array effects only play a minor role.

The reciprocity between incoming angle, focus location and emission angle, needed for the self-tracking, was verified on a hexagonal layer of 5  $\mu\text{m}$  diameter spheres on a glass substrate. The array is illuminated with plane wave excitation under increasing angle of incidence, from 0 to 45 degrees. The resulting field intensity in the substrate underneath the spheres is shown in Figure 2a–d. Upon increasing the angle of incidence in a clockwise direction, the hotspot moves toward the left. Subsequently, a second simulation is run, with a dipole emitter placed at the location of the hotspot (with the plane wave excitation turned off). The resulting emission patterns are shown in Figure 2e–h. Up to a 40 degrees angle of incidence excitation, there is an almost perfect correspondence between the excitation angle and the emission angle, as expected from reciprocity. At 45 degrees, the hotspot is moved almost a full sphere radius to the side, and thus moves underneath the neighboring sphere, as visible in Figure 2d. Emission from this hotspot location starts to couple to the next sphere, resulting in emission in the opposite direction of  $-45$  degrees, as visible in Figure 2h. The iodide-rich regions formed in the hotspot can thus follow the movement of the sun over a cone of  $\approx 80^\circ$ . This allows for automatic solar tracking without any mechanics having to be added to the modules, as the cone covers the brightest sun hours of the day.

We have investigated the potential solar cell performance of a mixed halide perovskite film with a monolayer of silica spheres through detailed optical and electrical simulations. The system under study consists of a 500 nm thick film of methylammonium lead iodide/bromide perovskite ( $\text{MAPb}(\text{I}_{0.5}\text{Br}_{0.5})_3$ ) on top of an aluminum back contact. This perovskite composition has a band gap of 1.9 eV, but under illumination nucleates a small amount of an iodide rich phase with a 1.7 eV band gap inside a high bandgap matrix.<sup>[18]</sup> As a top contact, a uniform

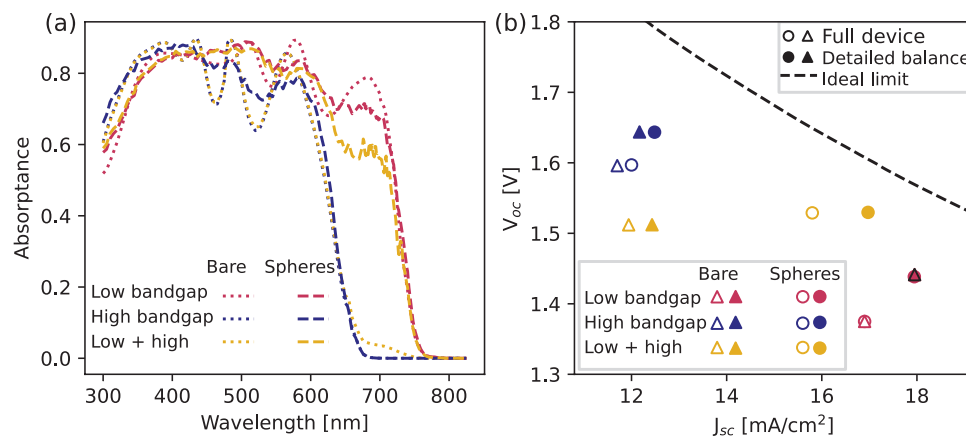


**Figure 3.** Absorption spectra and device performance simulation results for the six different systems: low bandgap (1.7 eV) film, high bandgap (1.9 eV) film, and phase segregated film with 3.6% low bandgap regions in a high bandgap film, each as bare film and with a monolayer of 5  $\mu\text{m}$  silica spheres on top. a) Absorption spectra obtained from FDTD simulations b) Open circuit voltage ( $V_{oc}$ ) and short circuit current ( $J_{sc}$ ) obtained from detailed balance calculations and full device simulations, based on the absorption spectra in (a). The black dotted line gives the ideal limit from detailed balance calculations assuming step-wise absorption onset, thus no tail states. The two-phase system with spheres approaches this limit most closely.

layer of indium-tin-oxide (ITO) is used, with a thin film of SU8 photoresist on top, which is needed for encapsulation and adhesion of the spheres. Although carrier selective contacts are not included in the optical model, in the ideal case they are only a few (5–15) nm thick and thus do not substantially affect the optical modeling. A hexagonal array of close-packed silica spheres forms the top layer. Since the ITO and SU8 have a refractive index in between those of the perovskite and air, these layers can also act as an anti-reflection coating. It was found that absorption in the perovskite is maximized for an ITO layer thickness of 50 nm and an SU8 layer thickness of 80 nm, where the lower limit of ITO thickness was set to 50 nm to ensure sufficiently low series resistance values (Figure S1, Supporting Information). For calculating the performance in the radiative limit, accurate modeling of  $J_0$  is required, as this limits the open circuit voltage.  $J_0$  is determined by the external quantum efficiency and the black body radiation spectrum.<sup>[19]</sup> Since the black body emission exponentially increases at lower energy,  $J_0$ , and thus  $V_{oc}$ , is very sensitive to the low energy tail states of the absorptivity/emissivity spectrum.<sup>[20]</sup> This is also the reason that halide segregation is usually undesirable in solar cells. Only one percent of a low bandgap phase can dominate the emission spectrum, even though the absorption hardly changes. This leads to voltage pinning, where the  $V_{oc}$  is limited by the low bandgap phase, but the absorption (and thus short-circuit current density,  $J_{sc}$ ) is still limited by the high band gap phase. Since the  $V_{oc}$  drops dramatically while the  $J_{sc}$  hardly increases, the overall efficiency drops substantially. Away from the radiative limit, non-radiative recombination becomes the dominant factor in limiting the voltage,<sup>[11]</sup> but for determining the ideal performance in the radiative limit, it is important to accurately model the absorption tail states of both unsegregated and segregated phases. Details on how this was done can be found in Supporting Information.

We have investigated perovskite solar cells made from phase separated films containing both low and high bandgaps as well as pure films of either the low or high bandgap. All of these cases are investigated with and without a mono-

layer of spheres, which allows us to separate the contribution of the different mechanisms that play a role in the final solar cell performance. We expect that in unsegregated films, the spheres will have almost no effect on efficiency since optical concentration does not change the total amount of absorption (no  $J_{sc}$  change) or carrier density (no  $V_{oc}$  change) in a spatially uniform film. Under illumination, we assume that photosegregation only occurs at the microlens focus and model this as 1  $\mu\text{m}$  diameter cylinders of low bandgap perovskite underneath each of the spheres in a matrix of high bandgap perovskite. This corresponds to the shape and size of the hotspot that is formed under broadband, plane wave illumination (Figure S2, Supporting Information), and thus how phase segregation is expected to occur. Without the spheres present, we keep the same phase separated structure—3.6% low bandgap material in a high bandgap matrix—such that there is electronic concentration (due to the different band gap) but no optical concentration. We assume that changes in the halide ratio in the high bandgap material are negligible, because of the small fraction of low bandgap phase that is formed. The resulting absorption spectra of all the cases above are shown in Figure 3a. With detailed balance calculations, for which the accurate modeling of the tail states was essential, the performance of these systems in the radiative limit is determined, as summarized in Table 2 and shown graphically in Figure 3b, filled markers.

It is insightful first to examine the performance of a bare phase segregated film. Compared to the high band gap reference film, photosegregation leads to a large drop in  $V_{oc}$  of 130 mV, due to the above-mentioned voltage pinning of the low bandgap phase. The increase in absorption above 650 nm is almost negligible, as can be seen in Figure 3a, resulting in only 0.2  $\text{mA cm}^{-2}$  increase in  $J_{sc}$ , and overall efficiency goes down by 1.2% absolute. Compared to the low bandgap reference film, photosegregation leads to a huge decrease in  $J_{sc}$  but a substantial increase in  $V_{oc}$  of 70 mV. The 3.6% of low bandgap phase hardly absorbs any light, limiting the  $J_{sc}$  to that of the high band gap, but provides a driving force for concentrating photogenerated carriers by a factor of 28. The observed increase

**Table 2.** Solar cell performance in the radiative limit as obtained from detailed balance calculations, based on the absorption spectra in Figure 3a. The phase segregation lowers  $V_{oc}$  and thereby efficiency, while spheres increase  $J_{sc}$  and efficiency. The combination of spheres and phase segregation gives rise to a large increase in both  $J_{sc}$  and  $V_{oc}$ , thanks to absorption enhancement and directional light emission, which results in a 6.6% higher efficiency compared to the segregated film without spheres.  $J_{sc}$  in  $\text{mA cm}^{-2}$ ,  $V_{oc}$  in V,  $\eta$  in %.

	Bare film			With spheres		
	$J_{sc}$	$V_{oc}$	$\eta$	$J_{sc}$	$V_{oc}$	$\eta$
Low bandgap (1.7 eV)	18.0	1.44	23.6	18.0	1.44	23.5
High bandgap (1.9 eV)	12.2	1.64	18.4	12.5	1.64	18.9
Low + high bandgap	12.4	1.51	17.2	17.0	1.53	23.8

in  $V_{oc}$  is similar to what would be expected for  $28\times$  concentration ( $k_B T/q \ln(28) = 86$  mV). It is important to note that in the radiative recombination limit this electronic concentration can never lead to efficiency improvements compared to the unsegregated high band gap film.

Now we examine the effect of adding spheres to each film. As anticipated, adding spheres to the low or high bandgap reference films has almost no effect on either the  $V_{oc}$  or  $J_{sc}$  and therefore does not change the efficiency (the  $0.3 \text{ mA cm}^{-2}$  increase in  $J_{sc}$  is due to a slight change in the reflection of the ITO/SU8 stack). In the segregated system, however, there is a large increase in both voltage and current when adding the spheres. The increase in  $J_{sc}$  can be attributed to the focusing by the spheres. The incoming sunlight is focused into the low bandgap perovskite, which gives a large increase in absorption between 650 and 750 nm, despite the fact that there is only 3.6% of the low bandgap phase present. This effective lowering of the bandgap should increase the thermal emission, but at the same time the directivity of the spheres should reduce the thermal emission by narrowing the emission cone (effective concentration). The result from these two competing effects is an increase in  $V_{oc}$  of 20 mV compared to the bare segregated film. The 90 mV increase compared to the low bandgap reference is also close to what is expected for an optical concentration of 51 ( $k_B T/q \ln(28) = 102$  mV), corresponding to that of the 5 micron spheres. Notably, the increase in  $J_{sc}$  when adding spheres only contributes slightly to the  $V_{oc}$  improvement ( $k_B T/q \ln(16.1/12.3) = 8$  mV), further supporting our claim that self-tracking optical concentration is responsible for the improvements. The spheres give an absolute 6.8% efficiency increase compared to the bare segregated film. The resulting efficiency of 23.8% is higher than that of both unsegregated reference films. The difference with the low bandgap film is relatively small, because the lenses do not focus all the incoming light

and thus the absorption between 680 and 780 nm is still not ideal. In an ideal scenario, our approach allows for optical concentration of direct solar photons with energy above that of the low bandgap and electronic concentration of diffuse solar photons with energy above that of the high bandgap, leading to an efficiency limit of about 33% for our 1.7/1.9 eV system (at maximum concentration), well above the 27% limit for a 1.7 eV cell without optical concentration. As we will see in the following, the concentrating effect of the spheres gives some additional benefit in the presence of non-radiative recombination, which makes the segregated system even more favorable over the low bandgap film. Also for application in tandem configurations, efficient high-bandgap perovskite solar cell designs are needed.

To obtain more realistic performance metrics, which include the effects of electrical contacts and non-radiative recombination, each of the above-mentioned devices is simulated in Lumerical Device CHARGE. The generation profile from the AM1.5 solar spectrum is obtained with the same optical FDTD simulations as the absorption spectra in Figure 3a and imported into Device. The electrical model includes hole and electron selective layers and planar contacts on each side. Details on the simulation and materials settings can be found in Supporting Information. The obtained performance metrics are summarized in Table 3 and shown graphically in Figure 3b, open markers. Starting again with the comparison of the films without spheres, we see that full device simulations including the effects of non-radiative recombination again lead to a reduced efficiency for the segregated film compared to either of the reference films. For these more realistic simulations, the  $V_{oc}$  and  $J_{sc}$  trends are the same as in the radiative limit case, but the drop in  $V_{oc}$  compared to the high band gap reference is smaller and the increase in  $V_{oc}$  compared to the low bandgap reference is larger, leading to smaller efficiency loss compared to the reference devices. This voltage improvement

**Table 3.** Solar cell performance in full device simulations, including non-radiative recombination as Shockley–Read–Hall recombination and surface recombination. Enhanced carrier concentrations due to the focusing of the spheres and funneling to the low bandgap regions drive the system toward more radiative recombination, resulting in less penalty in  $V_{oc}$  due to phase segregation. The segregated system with spheres gives the highest efficiency.  $J_{sc}$  in  $\text{mA cm}^{-2}$ ,  $V_{oc}$  in V,  $\eta$  in %.

	Bare film			With spheres		
	$J_{sc}$	$V_{oc}$	$\eta$	$J_{sc}$	$V_{oc}$	$\eta$
Low bandgap (1.7 eV)	16.9	1.38	20.2	16.9	1.38	20.1
High bandgap (1.9 eV)	11.7	1.60	16.3	12.0	1.60	16.7
Low + high bandgap	11.9	1.51	15.6	15.8	1.53	20.7

compared to the reference devices is caused by the combination of optical and electrical concentration, which lead to enhanced carrier concentration in the low-bandgap cylinders underneath the spheres. Increased carrier concentration causes the  $V_{oc}$  gain that is observed under optical concentration, also in the radiative limit. However, in the presence of non-radiative recombination, there is an additional benefit from increased carrier concentration. The dominant non-radiative recombination pathway, Shockley–Read–Hall recombination, scales linearly with carrier concentration. The radiative recombination rate scales with the carrier concentration squared. Higher carrier concentration thus pushes the system toward the radiative limit, increasing the internal quantum efficiency and thereby the voltage. In addition to optical concentration, our two gap system combined with the long diffusion lengths in perovskite allow for efficient electronic concentration. With the lifetime and mobility in the simulations of  $1 \mu\text{s}$  and  $15 \text{ cm}^2 \text{ V}^{-1} \text{ s}^{-1}$  respectively, the carrier diffusion length of  $7 \mu\text{m}$  is large enough compared to the radius of the sphere to enable effective excited state funneling into the low-bandgap regions at the sphere focus. Proof of this funneling effect was found by comparing the recombination rates in the segregated film without spheres to the low bandgap film without spheres. Since there is no optical focusing, absorption per unit volume in the low bandgap cylinders is the same as in the reference low bandgap film. However, carrier concentrations are up to an order of magnitude larger in the segregated film, which indicates that electrons and holes from elsewhere in the film recombine in the segregated regions. This funneling effect drastically reduces the influence of non-radiative recombination, as can be seen by comparing  $V_{oc}$  values in Tables 2 and 3.

## 2.2. Experiments

The optical effects of adding a monolayer of glass spheres on a perovskite film have also been demonstrated experimentally. A  $\text{MAPb}(\text{I}_{0.5}\text{Br}_{0.5})_3$  film was spin-coated on a glass substrate and encapsulated with a 15 nm aluminum oxide layer for enhanced stability as described before.<sup>[21]</sup> Monolayers of silica spheres were created with a simple rubbing technique, where

a dry powder of spheres was gently rubbed between two slabs of PDMS.<sup>[15]</sup> This resulted in large area (several square millimeters) monolayers of spheres on PDMS. The spheres do not stick well to the perovskite/alumina film, potentially due to the difference in hydrophobicity and the surface roughness of the film. Successful transfer to the perovskite film was obtained by spin coating two 100 nm thick layers of SU8 photoresist. The first layer flattens out any irregularities on the film and further protects the perovskite. Directly after spin coating the second layer and before curing it, the slab of PDMS with a monolayer of spheres is pressed into the film, by which the spheres stick into the photoresist and are transferred to the sample (Figure S3, Supporting Information). Attempts to use only a single layer of SU8 were unsuccessful; the force required to obtain a proper transfer damaged the perovskite film.

Accurate absorption spectrum measurements on the film with and without spheres, to verify the spectra in Figure 3a, were hindered by the high photoluminescence of the films, which keeps increasing under prolonged illumination (Figure S4, Supporting Information). This complicated accurate absorption measurements around the bandgap. Accurate absorption spectra at short wavelength were obtained using an integrating spheres setup as described before,<sup>[22]</sup> using short pass filters to remove any photoluminescence (PL) from the signals. Subsequently, simple transmission and reflection measurements were taken over the full spectrum with the detectors far away from the sample, to minimize PL signals. These measurements result in an anomalously high apparent absorption, because scattered light is not detected. By matching the spectrum to the integrating sphere measurements at short wavelengths, the amount of scattering could be determined. Assuming that this value is constant over the measured spectrum, accurate absorption values around the bandgap could be obtained from the transmission/reflection measurements, which are shown in Figure 4a. The film with spheres has higher absorption over the full spectrum compared to the bare film, due to a combination of focusing and anti-reflection effects of the spheres. At short wavelengths the focusing does not increase absorption, since these wavelengths are equally well absorbed in both high and low bandgap phase, so the 4% higher absorption can be fully attributed to anti-reflection effects (Figure S5, Supporting

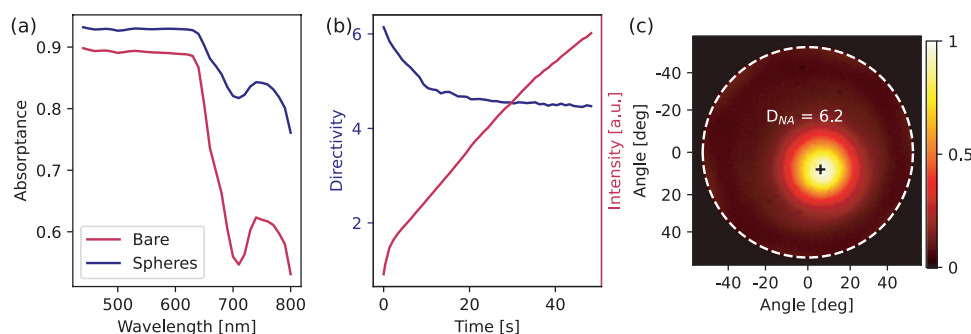


**Figure 4.** Experimental results on mixed halide perovskite films with a monolayer of silica spheres on top. a) Absorption spectra show an increase in absorbance over all wavelengths. At short wavelengths, this can be attributed to anti-reflection effects, while in the 700 to 800 nm range this can be attributed to focusing into the low bandgap regions underneath the spheres. b) Directivity and emission intensity as a function of time. Directivity decreases over time, potentially due to the segregated regions growing too large. c) Fourier image of the highest measured directivity of 6.2, in the numerical aperture of the objective ( $D_{NA}$ ).

Information). Toward the bandgap of the mixed-phase film, absorbance rapidly drops for the bare film, although there is a second bump in the absorption spectrum that corresponds to the absorption of the iodide-rich phase. In this spectral region, the film with spheres shows up to absolute 25% more absorption. This confirms the hypothesis that iodide-rich regions are self-aligned with the spheres, which focus the light into those regions, with a large increase in absorption as a result. The fact that for both samples absorption is higher than in the simulations indicates that there is more iodide-rich phase forming. Given the chemical flexibility of halide perovskites and the resulting effects on the light-induced phase separation, we expect that the size of the phase separation at a given light intensity can be controlled. The absence of the interference pattern in the bare film absorption, as seen in the simulations, can be explained by the surface roughness of the perovskite film, which was not taken into account in the simulations. Since this additional scattering increases absorption, this will have a positive impact on the device performance.

Directivity measurements were done with a Fourier microscopy setup, where a 515 nm wavelength fs laser was focused in the back-focal plane of the objective to ensure plane-wave illumination on the sample. The directivity of an ensemble of  $\approx 50$  spheres is measured (Figure S6, Supporting Information). The development of directivity and emission intensity over illumination time is shown in Figure 4b, with a Fourier image of the highest directivity measurement in Figure 4c. Upon initial illumination, the highest directivity of 6.2 is measured, but longer illumination results in a decrease in directivity. This trend is opposite of what would be expected and can be attributed to iodide-rich regions growing too big. Emission in the normal direction is only obtained from emission from the center of the spheres. If the iodide-rich region grows and emission happens from a large area underneath the sphere, directivity is decreased. This is in agreement with our absorption measurements in Figure 4a, where we also observed that more and/or larger iodide-rich regions are formed compared to our simulations. The directivity of 6.2 obtained here is the partial directivity within the numerical aperture of the objective, while the effective concentration is equivalent to the full directivity into the complete  $4\pi$  solid angle. The full directivity is expected to be higher, but measuring this is a more tedious task<sup>[23]</sup> and beyond the scope of this work. A more detailed discussion can be found in Supporting Information.

### 3. Conclusion and Outlook

In this work, we have shown how light-induced halide segregation in mixed halide perovskites can be exploited to improve solar cell performance. By placing a monolayer of silica microspheres on top of the perovskite layer, phase segregation can be controlled to take place in a highly functional manner. Each sphere focuses the incoming sunlight to a region where halide photosegregation occurs, forming a lower bandgap region that acts as a sink for excited states photogenerated by diffuse light in the high bandgap matrix. With optical simulations, we showed that the position of these focal points has a one-to-one mapping with the angle of incoming light, allowing for

self-optimized solar tracking for any angle between  $-40^\circ$  and  $40^\circ$ . When this system is applied in a solar cell, the focusing of the spheres causes an increase in  $J_{sc}$  of  $4.6 \text{ mA cm}^{-2}$  and an increase in  $V_{oc}$  of 40 mV in the radiative limit, resulting in an absolute increase in efficiency of 6.6%. In a complete device configuration, including non-radiative recombination and extraction losses, increases in  $J_{sc}$  and  $V_{oc}$  are  $3.9 \text{ mA cm}^{-2}$  and 20 mV respectively, and efficiency is increased by 5.1% absolute. While the low and high bandgap films show a voltage drop of 60 and 40 mV respectively when going from the radiative limit to the full device, the segregated films do not suffer from this reduction in  $V_{oc}$ . This can be attributed to additional benefits of the increased carrier concentration in the low bandgap regions, which push the system toward the radiative limit. Experimental verification showed that the presence of a monolayer of spheres on a perovskite film indeed increases the absorption significantly. This especially happens in the region between 650 and 800 nm, as light is focused on low bandgap regions that are formed in the film. Also, directional emission was observed experimentally, with partial directivity of 6.2.

A logical next step after these initial experimental proofs-of-concept is to measure full device performance. This requires the fabrication of a fully contacted device. Since the sphere monolayer can be simply added to the device at the end, via the same procedure as described for the optical experiments, full device fabrication is within reach. A more challenging aspect is the further optimization of the mixed halide perovskite film. Our experiments indicate that more phase segregation happens than what was assumed in the simulations. Some of this might be attributed to the relatively small excitation area used in experiments, which might cause the formation of iodide-rich regions everywhere in the illumination area, instead of only underneath the spheres (Figure S7, Supporting Information). The mixed halide perovskite films used here consist of very small grains, which give strong phase segregation. Larger grains might lead to less phase segregation, resulting in smaller emitters and higher concentration. However, initial experiments with large grain films resulted in rough films with large variations in PL intensity and spectrum throughout the sample, which complicated the transfer of spheres and optical characterization. By combining methods to control the phase segregation kinetics as a function of light intensity, for example by altering the A-site cation which drastically changes the ion photosegregation process, and further optimizing the iodide:bromide ratio for best performance, we see a path for the outstanding performance predicted by simulations to become reality.

Overall we can conclude that a simple, scalable technique of placing a monolayer of silica microspheres on top of a mixed halide perovskite film can significantly improve solar cell performance. A combination of anti-reflection and focusing effects causes an increase in  $J_{sc}$ . Directivity or concentration (thermodynamically equivalent) increase  $V_{oc}$ , with an additional boost in  $V_{oc}$  in the presence of non-radiative recombination due to increased carrier concentration, which pushes the system toward the radiative limit. This approach, in which we embrace the light-induced phase segregation rather than preventing it, can open up a new path for high-efficiency perovskite solar concentrators.

## 4. Experimental Section

**Chemicals:** MABr ( $\geq 98\%$ ), MAI ( $\geq 99\%$ ),  $\text{PbBr}_2$  ( $\geq 98\%$ ), and  $\text{PbI}_2$  ( $\geq 99.99\%$ ) were purchased from TCI. Chlorobenzene ( $\geq 99.8\%$ ) and dimethyl formamide (DMF, anhydrous  $\geq 99.8\%$ ) were purchased from Sigma-Aldrich. All chemicals were used as received.

**Substrate Preparation:** Fused quartz substrates of  $15\text{ mm} \times 15\text{ mm} \times 1\text{ mm}$  were cleaned with soap and subsequently sonicated in water, acetone, and isopropanol. The dried substrates were then UV/ozone treated for 20 min and quickly brought into a nitrogen glovebox afterward.

**MAPb( $\text{Br}_{0.5}\text{I}_{0.5}$ )<sub>3</sub> Thin Film Fabrication:** Film preparation took place in a nitrogen glovebox. An 0.64 M equimolar solution of MABr, MAI,  $\text{PbBr}_2$ , and  $\text{PbI}_2$  was made in DMF and stirred over night at  $70\text{ }^\circ\text{C}$ . The solution was filtered using a  $0.2\text{ }\mu\text{m}$  syringe filter. Thin films were then fabricated by spin coating  $80\text{ }\mu\text{L}$  of the precursor solution at 3000 rpm for 40 s. After 10 s,  $200\text{ }\mu\text{L}$  chlorobenzene antisolvent was dropcasted on the spinning sample. To crystallize, the sample was placed on a hot plate to anneal for 5 min at  $100\text{ }^\circ\text{C}$ .

**Encapsulation of Thin Films:** Encapsulation with  $15\text{ nm}$   $\text{Al}_2\text{O}_3$  was done using an electron beam physical vapor deposition system (Polyteknik Flextura M508E). Afterward, the films were coated with two layers of  $100\text{ nm}$  SU-8, obtained by a mixture of SU-8/cyclopentanone in a 1:10 ratio that was spin coated on at 4000 rpm for 30 s. The first layer was cured on a hot plate at  $100\text{ }^\circ\text{C}$  for 1 min, exposed to  $365\text{ nm}$  UV light for 5 min and again placed on the  $100\text{ }^\circ\text{C}$  hot plate for 1 min. Then the second layer was applied, and directly after spin coating a slab of PDMS with a monolayer of silica spheres was pressed into the soft SU8 and placed on a  $100\text{ }^\circ\text{C}$  hot plate for 1 min with a weight of  $160\text{ g}$  on top. The second layer was not cured with UV light to avoid damage to the perovskite film due to the focusing of the UV light by the spheres.

**Sphere Monolayer Self-Assembly:**  $5\text{ }\mu\text{m}$  diameter silica spheres in aqueous solution (Sigma Aldrich 44054-5ML-F) were dried to a powder on a hot plate. PDMS was mixed in a 1:9 ratio, poured into a petri dish and cured in the oven at  $80\text{ }^\circ\text{C}$  for 3 h. The cured PDMS was peeled off and cut into pieces of  $\approx 15 \times 15\text{ mm}$ . Some dry sphere powder was applied to one piece of PDMS and another piece was rubbed across with light finger pressure to spread out the spheres and form a monolayer.

**Absorption Measurements:** Absorption at short wavelength was determined with high accuracy using an integrating sphere setup described before,<sup>[22]</sup> using  $600\text{ nm}$  short pass filters to remove any PL from the signals. The full absorption spectrum up to  $800\text{ nm}$  wavelength was measured with transmission and reflection measurements with a Thorlabs amplified Si detector (PDA100A) for the reflection signal and a passive Newport 818-UV photodetector for the transmitted signal, both read out by Stanford Research Systems SR830 lock-in amplifiers. The sample was excited using a supercontinuum laser (NKT Fianium FIU 15) and acousto-optical tunable filters to select  $\approx 2\text{ nm}$  bandwidth light in steps of  $10\text{ nm}$  from  $400$  to  $800\text{ nm}$ .

**Fourier Measurements:** Fourier images were taken in a home built inverted Fourier microscopy setup. The sample was excited with a pulsed laser at  $1\text{ MHz}$  with  $150\text{ fs}$  pulses and of  $515\text{ nm}$  wavelength. The laser was focused on the back-focal plane of a  $100 \times 0.85\text{ NA}$  objective (CFI L Plan EPI CRA), to obtain a collinear spot of  $\approx 60\text{ }\mu\text{m}$  in diameter on the sample plane. Through the same objective, light emission from the sample was collected, and by placing a lens in the imaging path in focus with the back-focal plane of the objective, via a 1:1 telescope, Fourier images were obtained, as in ref. [24]. The pump was filtered from the PL signal with a combination of a  $514\text{ nm}$  dichroic and a  $550\text{ nm}$  long-pass filter. The Fourier images were taken with a Thorlabs CS2100M-USB camera.

## Supporting Information

Supporting Information is available from the Wiley Online Library or from the author.

## Acknowledgements

This work is part of the research programme Mat4Sus, which is financed by the Netherlands Organisation for Scientific Research (NWO). The work has been carried out at AMOLF, an NWO funded institute.

## Conflict of Interest

The authors declare no conflict of interest.

## Data Availability Statement

The data that support the findings of this study are available from the corresponding author upon reasonable request.

## Keywords

concentrator photovoltaics, microspheres, mixed halide perovskites

Received: August 29, 2022

Revised: January 20, 2023

Published online:

- [1] Best Research-Cell Efficiency Chart, <https://www.nrel.gov/pv/cell-efficiency.html> (accessed: March 2022).
- [2] J. S. Van Der Burgt, E. C. Garnett, *ACS Photonics* **2020**, *7*, 1589.
- [3] G. Smestad, H. Ries, R. Winston, E. Yablonovitch, *Sol. Energy Mater.* **1990**, *21*, 99.
- [4] A. K. Jena, A. Kulkarni, T. Miyasaka, *Chem. Rev.* **2019**, *119*, 3036.
- [5] W. J. Yin, T. Shi, Y. Yan, *Adv. Mater.* **2014**, *26*, 4653.
- [6] S. Sun, T. Salim, N. Mathews, M. Duchamp, C. Boothroyd, G. Xing, T. C. Sum, Y. M. Lam, *J. Energy Environ.* **2014**, *7*, 399.
- [7] J. H. Noh, S. H. Im, J. H. Heo, T. N. Mandal, S. I. Seok, *Nano Lett.* **2013**, *13*, 1764.
- [8] W. Mao, C. R. Hall, S. Bernardi, Y. B. Cheng, A. Widmer-Cooper, T. A. Smith, U. Bach, *Nat. Mater.* **2021**, *20*, 55.
- [9] D. T. Limmer, N. S. Ginsberg, *J. Chem. Phys.* **2020**, *152*, 230901.
- [10] A. F. Gualdrón-Reyes, S. J. Yoon, I. Mora-Seró, *Curr. Opin. Electrochem.* **2018**, *11*, 84.
- [11] S. Mahesh, J. M. Ball, R. D. Oliver, D. P. McMeekin, P. K. Nayak, M. B. Johnston, H. J. Snaith, *J. Energy Environ.* **2020**, *13*, 258.
- [12] K. W. Allen, A. Darafsheh, V. N. Astratov, in *2011 13th International Conference on Transparent Optical Networks*, IEEE, Piscataway, NJ **2011**, pp. 1-4.
- [13] B. S. Luk'yanchuk, R. Paniagua-Domínguez, I. Minin, O. Minin, Z. Wang, *Opt. Mater. Express* **2017**, *7*, 1820.
- [14] W. Stöber, A. Fink, E. Bohn, *J. Colloid Interface Sci.* **1968**, *26*, 62.
- [15] C. Park, T. Lee, Y. Xia, T. J. Shin, J. Myoung, U. Jeong, *Adv. Mater.* **2014**, *26*, 4633.
- [16] S. A. Mann, R. R. Grote, R. M. Osgood, A. Alù, E. C. Garnett, *ACS Nano* **2016**, *10*, 8620.
- [17] J. E. Haverkort, E. C. Garnett, E. P. Bakkers, *Appl. Phys. Rev.* **2018**, *5*, 031106.



- [18] E. T. Hoke, D. J. Slotcavage, E. R. Dohner, A. R. Bowring, H. I. Karunadasa, M. D. McGehee, *Chem. Sci.* **2015**, *6*, 613.
- [19] T. Kirchartz, U. Rau, *Adv. Energy Mater.* **2018**, *8*, 1703385.
- [20] J. Wong, S. T. Omelchenko, H. A. Atwater, *ACS Energy Lett.* **2021**, *6*, 52.
- [21] J. S. van der Burgt, F. Scalerandi, J. J. de Boer, S. A. Rigter, E. C. Garnett, *Adv. Funct. Mater.* **2022**, *32*, 2203771.
- [22] S. A. Mann, B. Sciacca, Y. Zhang, J. Wang, E. Kontoleta, H. Liu, E. C. Garnett, *ACS Nano* **2017**, *11*, 1412.
- [23] J. S. Van Der Burgt, C. D. Dieleman, E. Johlin, J. J. Geuchies, A. J. Houtepen, B. Ehrler, E. C. Garnett, *ACS Photonics* **2021**, *8*, 1143.
- [24] I. Sersic, C. Tuambilangana, A. F. Koenderink, *New J. Phys.* **2011**, *13*, 083019.